# Modeling of Void Formation in Phase Change Memory Devices

Adam Cywar, Zachary Woods, SangBum Kim, Matt BrightSky, Norma Sosa, Yu Zhu,
Hyeong Soo Kim, Hyung Keun Kim, Chung Lam, Ali Gokirmak and Helena Silva

***Abstract*— An empirical versatile finite-element model is developed to predict void formation in as-deposited or melt-quenched amorphous $Ge_2Sb_2Te_5$ during annealing. This model incorporates void formation with nucleation and growth of the crystals along with thermal models that capture laser heating of the nano-structures during device fabrication. Modeling of void formation during Joule heating or furnace annealing can be implemented in a similar way. The modelling results are compared to example experimental results obtained from pore-cell phase change memory structures.**

***Index Terms* — phase-change memory; void formation; crystallization; amorphization; laser annealing; GeSbTe.**

## I. Introduction

Phase change memory (PCM) is a resistive memory technology that utilizes the resistance contrast between the amorphous and crystalline phases of a chalcogenide material, typically a GeSbTe (GST) ternary alloy.[1]–[3] This material can be reversibly and rapidly switched between the two phases by self-heating via electrical pulses. A reset operation refers to the crystalline-to-liquid followed by liquid-to-amorphous phase transitions, achieved by a short, high amplitude and abrupt ending pulse. Set operation refers to the amorphous-to-crystalline transition achieved by a lower amplitude, longer duration pulse. While PCM can be monolithically integrated with CMOS for system-on-chip approaches, there are materials and processing challenges. One of the biggest challenges that impact large-scale manufacturability is the volume change of as-deposited amorphous GST during heating and crystallization which typically leads to formation of multiple voids. Similarly, voids also form as the devices are cycled between solid and liquid phases during normal operation. Depending on their locations and sizes these voids may strongly affect device performance and reliability. Modeling the volume change and void formation during crystallization will help design experiments to determine the most favorable process conditions or device geometries.

Efficient models for crystallization of GST that have been reported in the literature [4]–[6] do not account for the ~ 6.5% volume reduction that occurs upon the as-deposited amorphous to crystalline phase change [7]. On the other hand, fundamental models of void distributions in GeTe alloys based on density functional and molecular dynamics simulations [8], [9] cannot be coupled with electro-thermal device models due to computation complexity.

In this work, we describe an empirical model that captures the volume change and void formation in as-deposited or melt-quenched GST upon crystallization, and builds upon our existing effective media approximation and discrete grains models.[10][11] The difference in crystallization time for as-deposited and melt-quenched amorphous GST is captured through an incubation period model. We compare the modeling results with example experimental results obtained from laser annealed GST pore-cells.

## II. Experiment

An experiment is performed to crystallize and densify as-deposited GST in pore cells to prevent excessive voids from forming during subsequent device operation. Laser annealing is used, instead of conventional annealing in a furnace, to explore the effect of a large temperature gradient from the wafer surface to the substrate, and examine the possibility of crystallization starting from one end of the cell leading to localization of the voids. Atomic layer deposition (ALD) is used to deposit N-doped amorphous GeSbTe ($GST_{ALD}$) within the pore cells. Transmission electron micrograph (TEM) of an empty pore cell structure is shown in Fig 1(a). An Ultratech Laser Anneal system is used to modulate and scan a 532 nm (green) laser across the field of PCM cells. The laser spot in the experiments is ~ 10 μm in the direction of the scan and ~ 1 mm wide in the orthogonal direction to the scan.

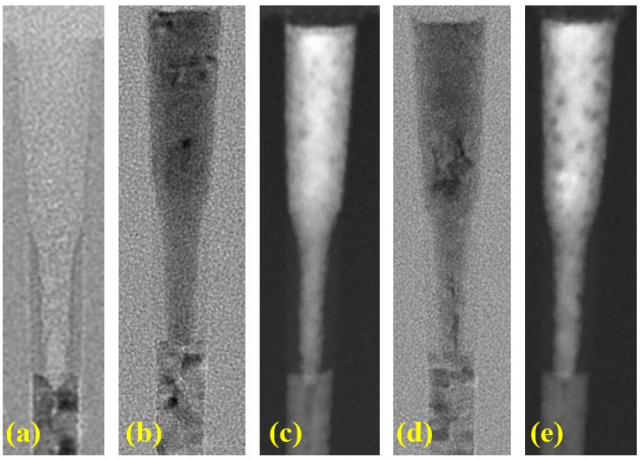


Figure 1. (a) TEM of an empty pore cell structure. (b) TEM and (c) STEM of cells annealed with a single laser pulse, and (d) TEM and (e) STEM of cells annealed with multiple laser pulses.

This work was supported by the National Science Foundation through the Graduate Research Fellowship Program (A. Cywar) and through awards ECCS 1150960 (A. Gokirmak) and DMR 1710468 (H. Silva). A. Cywar, Z.Woods, A. Gokirmak and H. Silva are with the Electrical and Computer Engineering Department, University of Connecticut, Storrs, CT 06269 USA. E-mail: helena.silva@uconn.edu. S. Kim, M. BrightSky, N. Sosa, Y. Zhu and C. Lam are with the IBM Watson Research Center, Yorktown Heights, NY, USA. H. S. Kim and H. K. Kim are with SK Hynix, 2091, Gyeongchung-daero, Bubal-eub, Icheon-si, Gyeonggi-do, Korea.

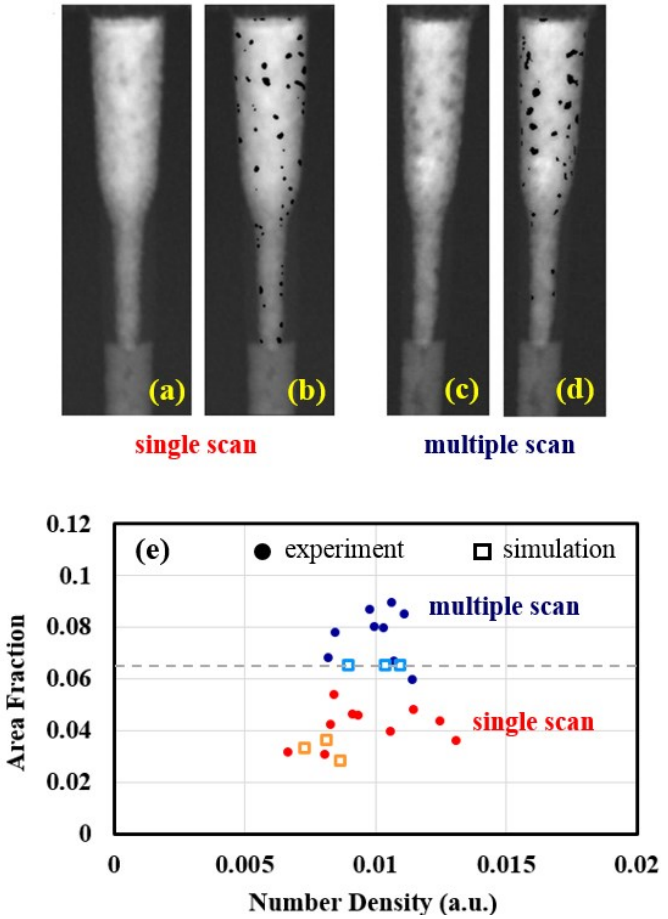


Figure 2. STEM images of laser annealed cells with a single scan (a) and highlighted void areas (b), and with multiple scans (c) and highlighted void areas (d). Distribution of experimental area fraction and number density of voids in the cells (solid circles), together with the simulation results discussed later (open squares). The dotted line indicates 0.065 void area fraction, which corresponds to the ~6.5% density change in the material that the model is designed to achieve as the crystal fraction reaches 100%.

The laser is pulsed for 50 ns durations with a frequency of 10 kHz at a scan rate of 167 mm/s. The substrate is held at ~ 525 K and laser pulses with energy per area of ~ 1.589 mJ/mm$^2$ are delivered to the wafer. Experimental results from a single scan are shown in Fig 1(b,c), and from 5 scans shown in Fig 1(d,e). High-magnification TEM images suggest that single scans of amorphous cells typically result in ~ 25% crystallization fraction and multiple scans are required to achieve full crystallization. STEM images shown in Fig 1(c,e) show the void locations that occurred during the first-time crystallization of these cells for the single and multiple scan cases, respectively, with larger and more apparent voids appearing in the multiple scan case. The simulation results, discussed later, show that for the laser power used in the experiments, the peak temperature on the wafer surface is approximately equal to the melting temperature of the phase-change material, but the pore cells, beneath the silicon dioxide capping layer, remain at lower temperatures and no melting is expected during the laser anneals. Fig. 2 highlights void locations for the single and multiple scan cases and the area fraction and number density of the voids in various cells, obtained using ImageJ processing software. Cells in the single scan case have less void area than in the multiple scan case, as expected since there is less crystallization and thus less volume change in the material. However, the number of voids observed in the two cases is approximately the same. This may be due to close-by small voids coalescing together into a larger void, as previously observed in GST [12], single voids becoming larger due to the volume change as neighboring grains grow further, and also increased strain due to higher Young's modulus of crystalline GST compared to that of amorphous GST [13].

## III. Crystallization Model

Our existing models capture the amorphous-to-crystalline phase change as well as the liquid to amorphous phase change, allowing for simulations of set-reset cycling of devices under joule heating (self-heating).[10][11] This approach can also be used to model the crystallization of a GST nanostructure under laser annealing or furnace annealing, showing where crystallization is expected to start from and the expected final distribution of grains. Modeling the amorphous to crystalline phase change is achieved by simulating the nucleation and growth of crystal grains within an amorphous matrix. Nucleation and growth rates in the GST at each mesh point and each timestep in the simulation are calculated based on the temperature, using the literature data for temperature dependent nucleation and growth rates [6]. For sputtered $GST_{225}$ the nucleation rate is highest at ~ 600 K and diminishes at higher temperatures where the growth velocity is largest, ~750 K (Fig 3). Estimates for the nucleation and growth rates for the $GST_{ALD}$ material are also shown in Fig 3 and are discussed further in Section V. Crystal nuclei are generated via a probability function based on the nucleation rate, mesh size and timestep in the simulation, and expand into crystal grains according to the growth rate. Amorphization of crystalline material is modeled by resetting the phase to amorphous for any GST that has exceeded the melting temperature. A crystal density variable *CD* is assigned to each mesh point in the GST, where a value of zero or one represents amorphous or crystalline material, respectively, allowing for dynamic updates of the material parameters during the simulation. Amorphous material properties for GST are used for locations where *CD* = 0 and likewise crystalline properties are used for locations where *CD* = 1. Using the local crystal density variable *CD* to represent the dynamically changing grain shapes and material properties within one heavily meshed domain is simpler and more efficient than generating separate individually meshed domains for the grains. The rate equation for *CD* is given by:

$$\frac{dCD}{dt} = Nuc(T, CD) + Grow(T, CD) + Amorph(T, CD) \qquad (1)$$

with the Nucleation, Growth and Amorphization functions given by the following:

$$\mathrm{Nuc}(T, CD) = \mathrm{N}(T)\,(1 - CD)\,\mathrm{e}^{\frac{1}{CD+0.3}}\,\mathrm{rnd}(x, y, t) \tag{2}$$

$$\mathrm{N}(T) = \mathrm{e}^{\frac{-(T-\alpha_1)^2}{\alpha_2}}\,\mathrm{ns}^{-1} \tag{3}$$

$$\mathrm{Grow}(T, CD) = \mathrm{G}_{\mathrm{InMesh}}(T, CD) + \mathrm{G}_{\mathrm{InterMesh}}(T, CD) \tag{4}$$

$$G_{InMesh}(T, CD) = \alpha_3 v_G(T) F_1(CD) \tag{5}$$

$$\mathrm{F}_1(CD) = \left(\frac{-2}{1 + \mathrm{e}^{CD+0.1}} + 1\right)\mathrm{F}_{\mathrm{Stability}} \tag{6}$$

$$F_{Stability} = \left(\alpha_4 \mathrm{e}^{-(CD-0.5)^2} + \alpha_5\right) \tag{7}$$

$$\mathrm{G}_{\mathrm{InterMesh}}(T, CD) = \alpha_6 v_G(T)\left(1 + \mathrm{e}^{\frac{CD-0.5}{0.1}}\right)^{-1} \nabla^2 CD \tag{8}$$

$$\mathrm{Amorph}(T, CD) = CD\left(\frac{1}{1 + \mathrm{e}^{\frac{T-873}{0.5}}} - 1\right)\mathrm{ns}^{-1} \tag{9}$$

where $t$ is the time and $T$ is the temperature. The rationale for these functions and different constants $\alpha_i$ used are explained in detail in Refs. [10] and [11]. In the nucleation term, a random number between 0 and 1 is generated at each mesh point for every timestep, *rnd(x,y,t)*, and is compared to the nucleation probability at that mesh point, where the nucleation probability is equal to the nucleation rate [$nm^{-3}s^{-1}$] times the mesh size [$nm^3$] times the timestep [s]. The growth term grows the nucleated grains at a rate equal to the temperature dependent growth rate (Fig 3). The amorphization term forces *CD* to 0 for temperatures above the melting temperature ($T_{melt}$ = 873 K). The stability term is used to ensure that the value of *CD* does not increase to greater than 1 or less than 0, as the model is using a binary representation of amorphous and crystalline areas for *CD* = 0 or 1, respectively. The stability term is essentially a snap-function – the term becomes very large, positive if *CD* is less than zero or becomes very large, negative if *CD* is greater than 1, "snapping" the values to either 0 or 1. Likewise, values that are in between 0 and 1 are snapped toward the closer value. Grain boundaries can be distinguished by tracking the locations which have both high d*CD*/dt and high d*CD*/dx rates.

Figure 4 shows simulation results from this model and from the crystallization model of Burr et al. [6] from which our nucleation and growth rates are taken. The temperature-time conditions used in our simulations are the same as the conditions in [6]. There is good agreement between the two models' results despite the fundamental differences in the computational approaches, as Burr *et al.* use a complex cellular automata approach that calculates surface energy density and bulk free energy difference between the crystal grains and surrounding amorphous area. In this work we introduce an additional variable, incubation time, to model the differences between as-deposited and melt-quenched amorphous material.

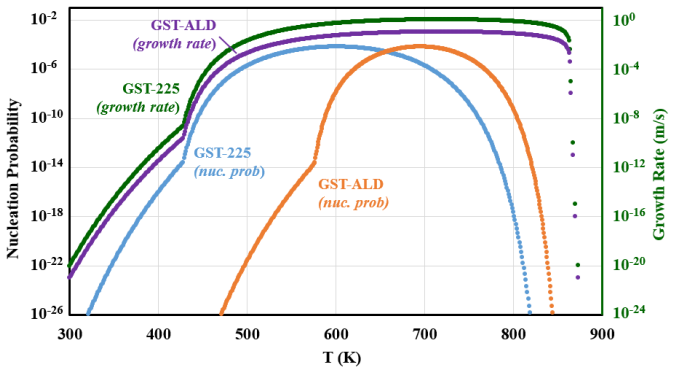


Figure 3. Nucleation probabilities derived from the nucleation rates for PVD $GST_{225}$ [5] (blue) and estimated for $GST_{ALD}$ (orange), with 5 ns time intervals and a 1 $nm^2$ 2-D mesh with 10 nm depth in a 2-D planar simulation. Growth velocity for $GST_{225}$ (green) is taken from [5] and estimated for $GST_{ALD}$ (purple).

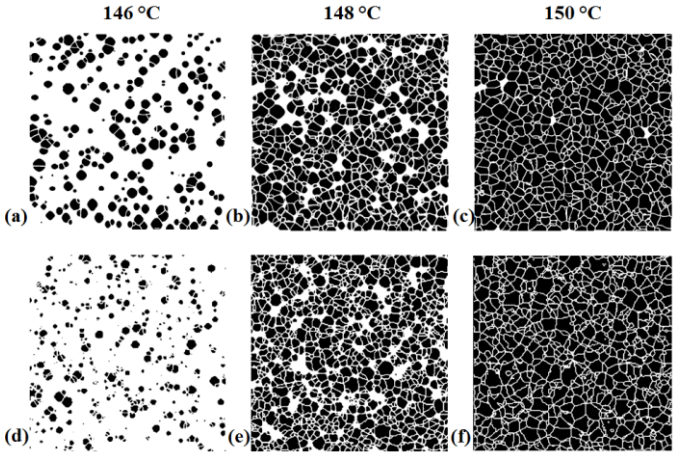


Figure 4. Comparison of simulation results from our nucleation and growth model (a-c) with those from Burr et al. [6] (d-f) at various temperatures achieved during a 1.3 C/s heating ramp. Figure from [11].

Our nucleation probabilities are derived from steady-state values [6], but according to the generally accepted view, an incubation time [14]–[16] must also be accounted for in transient simulations of as-deposited amorphous material. Melt-quenched amorphous material has been shown to crystallize quickly due to the presence of quenched-in nuclei [16]–[18], whereas the as-deposited material requires additional time to overcome the thermodynamic barrier to nucleation in which the subcritical clusters become stable [14]–[16]. Temperature dependent incubation times for as-deposited amorphous GST ($t_{inc}(T)$) have been reported in the literature by Weidenhof et al. [16]. To capture this phenomenon in the model, an *incubation* variable is introduced to keep track of the thermal history of each mesh point by integrating $t_{inc}(T)$ over time (Fig 5).

The use of an 'incubation time' is equivalent to using a lower nucleation probability for as-deposited amorphous material, compared to that for melt-quenched amorphous material. The rate equation for the *incubation* variable is given by:

$$\frac{dIncubation}{dt} = \frac{(1 - CD)}{t_{\mathrm{inc}}(T)} - Incubation.\,(Step\_melt(T)) \tag{10}$$

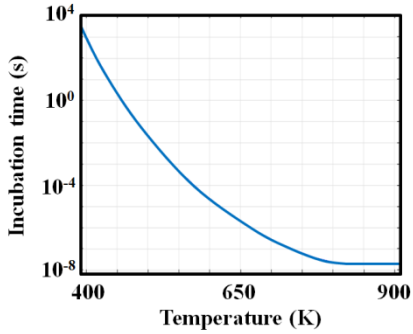


Figure 5. Incubation time $t_{inc}(T)$ vs. temperature curve used in the simulations, indicating the time for formation of sub-critical nuclei in as-deposited amorphous GST.

Here, *Step_melt*(T) resets the *incubation* variable to 0 for mesh points whose temperatures are greater than the melting temperature. We have slightly altered the behavior of $t_{inc}(T)$ from Ref. [16] in the high temperature range so it continues to decrease and saturates at a minimum value of 20 ns close to the melting temperature, instead of increasing at 825 K (Fig. 5).

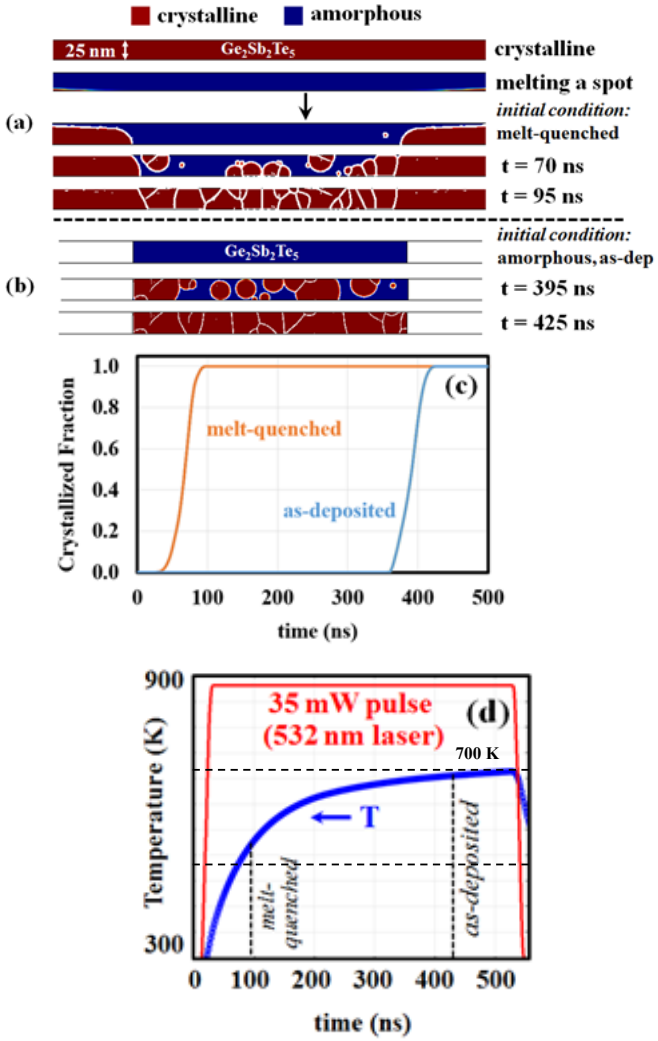


Figure 6. Simulation results comparing crystallization of melt-quenched (a) and as-deposited GST (b). The GST film is 25 nm thick and crystallization occurred during a 35 mW green laser pulse. Crystallized fraction versus time (c) and temperature of the center of the GST region versus time during the laser anneal (d). The dotted lines indicate the crystallization times of the melt-quenched and as-deposited films.

This change is made to allow the incubation variable to quickly increase when cooling from melt to reflect the presence of quenched-in nuclei and higher structural order of melt-quenched GST that is observed and reported in the literature [18], [19]. The *incubation* variable is used to scale the steady state nucleation probabilities when the incubation variable is less than 1, thus resulting in little to no nucleation of crystal grains until the thermodynamic barrier to nucleation is overcome.

Figure 6 shows simulation results of crystallization of melt-quenched and as-deposited GST. The initially crystalline GST is melt-quenched by a 60 ns, 75 mW laser pulse ($T_{film} > T_{melt}$), cooled to room temperature, and then annealed with a 100 ns, 35 mW green laser pulse. The laser heating model is described in detail in the next section. Fig 6(a) shows the melt-quenched amorphous spot (~ 320 nm wide), with a small (< 5 nm) quenched-in nucleus that formed during cooling from melt. Nucleation and growth occur quickly during the crystallization pulse, with crystallization of the spot completed in ~ 100 ns. For comparison, we have simulated the crystallization of a 320 nm wide spot in an as-deposited GST film with a longer 35 mW pulse laser anneal (Fig 6(b)). The crystallization times obtained for the melt-quenched and as-deposited GST films, ~100 ns and ~400 ns, Fig. 6(c), are in agreement with experimental results from the literature for crystallization of melt-quenched and as-deposited GST films of similar thicknesses under similar laser conditions [20]. The crystallization curves for the as-deposited and melt quenched GST have approximately the same shape, due to the same nucleation and growth rates used, but are shifted in time by the incubation period introduced to capture the delay in nucleation events for as-deposited GST. Temperature-time characteristics taken from the center of the GST spots are shown in Figure 6(d). The temperature in the film during crystallization is higher for the as-deposited case, as the incubation time must be overcome, resulting in a slightly lower number of slightly larger grains due to the changes in nucleation and growth rates between these temperatures.

## IV. Laser Model

Laser annealing is usually modeled as a heat source that is a function of location and of the absorption and reflection coefficients of the materials:

$$Q = Q_0 \cdot (1 - R_C) \cdot \frac{A_C}{\pi \cdot \sigma_x} e^{-\frac{x^2}{2\sigma_x^2}} \cdot e^{-A_C \cdot y} \qquad (11)$$

where y is the vertical position from the surface of the wafer into the substrate, x is the horizontal position from the center of the laser spot, and *d* is the assumed depth of the 2-D planar simulation (10 nm), $A_C$ is the absorption coefficient, $R_C$ is the reflection coefficient, and $\sigma_x$ is the standard deviation of the laser power distribution in the x direction. Parameters $A_C$ and $R_C$ for amorphous and crystalline GST at 532 nm wavelength are shown in Table 1. $A_C$ and $R_C$ values used for TiN, $SiO_2$, and Si at this wavelength are 2.8 x $10^7$ $m^{-1}$ and 0.38, 50 $m^{-1}$ and 0.05, and 3 x $10^5$ $m^{-1}$ and 0.34, respectively. For the simulations shown in Fig 6, $\sigma_x = 1$ µm and $Q_0 = 35$ mW, typical values for

laser crystallization experiments with a similar wavelength laser [20]. This applied power heats the film to ~ 600 K, where the nucleation rate in GST is maximum.

Since the laser spot size, ~ 10 µm, is significantly larger than the $GST_{ALD}$ PCM devices and simulation areas, the Gaussian distribution term in the lateral direction is dropped:

$$Q = Q_0 \cdot (1 - R_C) \cdot \frac{A_C}{X \cdot d} \cdot e^{-A_C \cdot y} \qquad (12)$$

where $X$ is the total width of the simulation area.

Power distribution is assumed to be uniform, based on the energy/area values used in the experiments [20]:

$$Q_0[W] = \frac{energy}{area}\left[{}^{J}/_{m^2}\right] \cdot \frac{1}{t_{pulse}}\left[{}^{1}/_{s}\right] \cdot X \cdot d\ [m^2] \qquad (13)$$

The laser anneal is modeled as a stationary 50 ns pulse with 10 ns rise and fall times since the laser spot size is very large in comparison to cell dimensions and the duty cycle and frequency are low (0.05% ON time, 100 µs period). The crystallization and void formation models are applied to a single PCM cell only, which is meshed heavily (~ 1 $nm^2$ elements). A simulation result of the laser anneal with the same parameters as in the experiments is shown in Fig 7, illustrating the large temperature gradient in the PCM cells as a result of the large absorption coefficient of GST and the exponential decay of the heat source in the $y$ direction.

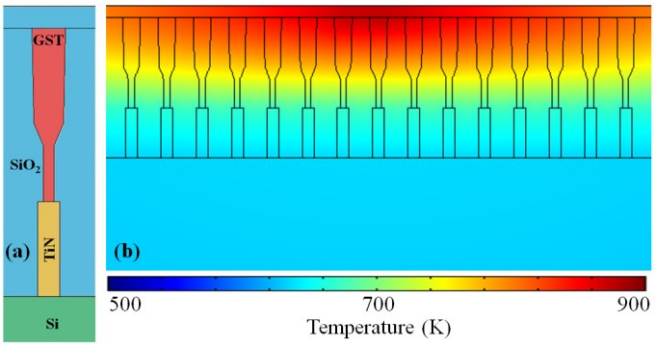


Figure 7. (a) Simulated PCM cell materials and geometry, and (b) temperature profile of the wafer during the peak temperature in the laser anneal. The TiN heater diameter is 20 nm.

## V. Void Formation Model

Although the confined PCM cell is an attractive design for PCM due to reduced reset current, small device pitch, and multi-bit storage capabilities, several fabrication challenges and reliability issues need to be overcome. The density difference between the different phases of GST material – especially between the as-fabricated amorphous phase and the crystalline phase [7] – together with the stochastic nature of grain nucleation, result in disseminated voids within the devices that may lead to failures. An accurate void formation model can be used to design fabrication and programming techniques toward void-free devices.

A solid mechanics model is incorporated in the simulations to calculate the stress within the phase-change material as it heats and crystallizes[21]. The thermal, mechanical and optical properties used in the model are shown in Tables 1 and 2. It has been reported that the volume reduction of the crystalline phase in GST results in deformation of the material leading to dislocations and increased stress, especially at grain edges [22], [23]. It is also known that in other polycrystalline materials stress-induced void formation typically occurs at the grain boundaries[24], [25]. Considering this behavior, the initial void formation in this model is set to occur at grain boundaries or at the device sidewall interfaces once a significant amount of crystallization has taken place (> 15%). Specific locations for boundaries or sidewall interfaces are determined using a stochastic process similar to the crystal grain nucleation algorithm, but in this case the probability of occurrence is

| | $GST_{225}$ Material Properties | Amorphous | Crystalline (FCC) |
|---|---|---|---|
| Thermal | Heat Capacity (J / kg·K) | 202* | 202* |
| | Thermal Conductivity (W / m·K) | 0.2 | ~ 0.5 - 1.7 (T-dep.) |
| | Density ($kg/m^3$) | 5870 | 6270 |
| Mechanical | Coefficient of Thermal Expansion x $10^{-6}$ (1/K) | 13.3 | 17.4 |
| | Poisson Ratio (unitless) | 0.275 | 0.255 |
| | Young's Modulus (GPa) | 24.8 | 39.5 |
| Optical | Absorption Coefficient (1/m) | 5 x $10^7$ | 1 x $10^8$ |
| | Reflection Coefficient (%) | 42 | 51 |

Table 1. Material parameters used for amorphous and crystalline GST in the simulations [7], [13], [26]–[29]. *A large spike in heat capacity at the melting temperature is included to model the latent heat of fusion as shown in Ref [30]. Temperature dependent thermal conductivity can also be seen in Ref [31].

| | TiN | $SiO_2$ | Si |
|---|---|---|---|
| Coefficient of Thermal Expansion x $10^{-6}$ (1/K) | 7.1 | 0.55 | 2.6 |
| Poisson ratio (unitless) | 0.199 | 0.17 | 0.28 |
| Young's Modulus (GPa) | 676 | 73.1 | 170 |

Table 2. Mechanical parameters used for TiN, SiO2 and Si in the simulations.

determined by the von Mises stress (indicating distortion energy) rather than temperature. Existing voids expand at a rate based on the relative von Mises stress in the material as well as the rate of crystallization, as the volume reduction in the crystallized material is the driving force behind the void formation. Like in the crystallization modeling method, a local void variable $\boldsymbol{\varphi}$ represents a void or non-void location with a value of 1 or 0, respectively, and the rate equation is given by:

$$\frac{d\varphi}{dt} = Nuc(CD, \varphi, GB) + Grow\ (CD, \varphi, \sigma) \qquad (14)$$

where σ is the von Mises stress. The nucleation term represents void formation at grain boundaries, *GB*, as grains grow together. The growth term, which includes a stability term as before, represents the growth of voids at a rate proportional to stress and the crystallization rate. The rate equation achieves and maintains the relationship $\boldsymbol{\varphi}_{avg} = CD_{avg} \cdot 6.5\%$ in the PCM cell domain to satisfy conservation of mass as the GST crystallizes.

The nucleation and growth rates for N-doped $GST_{ALD}$ are estimated based on data available for sputtered $GST_{225}$ (Fig 3) together with experimental observations of differences between

N-doped $GST_{ALD}$ and sputtered $GST_{225}$. It was observed that $GST_{ALD}$ begins to crystallize at ~ 575 K, ~150 K higher than what is observed for sputtered $GST_{225}$ (~ 425 K). The nucleation probability curve for $GST_{ALD}$ is therefore estimated by shifting the curve for $GST_{225}$ by 150 K and scaling it so that is also drops off before the melting temperature. Additionally, N-doping of GST was observed to significantly slow down the crystallization speed [15, 16], hence the growth rate of the N-doped $GST_{ALD}$ is estimated by scaling the curve for $GST_{225}$ by an order of magnitude. These estimated rates give simulation results of crystallized fraction and number of grains that are in general agreement with experimental observations (Fig. 2e).

Simulation results of crystallization and void formation during the laser anneal are shown in Fig 8, alongside example experimental results. Figs 8(c,d) illustrate how void formation

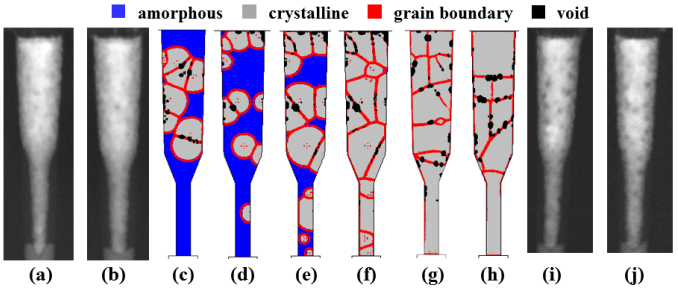


Figure 8. (a,b) Example STEM image of cells after a single scan laser anneal. (c,d) Simulation result of crystallization and void formation in two cells for a single scan. (e) Simulation result for the cell shown in (d) after a second scan, and (f) after a third scan. (g,h) Additional simulation results of cells for multiple scans and (I,j) STEM images of cells after multiple scans.

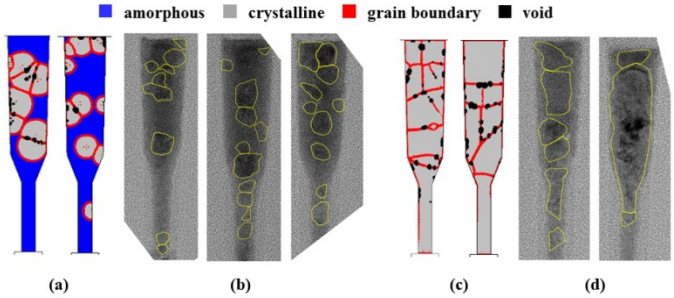


Figure 9. (a) Simulation result and (b) example TEM images showing experimental result of cells for the single scan laser anneal. (c) Simulation result and (d) TEM images showing experimental result of cells for the multiple scan laser anneal. In the TEM images, crystal grains are shown with a yellow outline, determined from higher magnification inspection from high resolution TEM.

is captured in the model, with the voids appearing at the boundaries of the growing grains after a single laser scan. The evolution of crystallization after a second scan (Fig. 8e) and after a third scan (Fig. 8f) result in the expansion of existing voids as well as the formation of new voids.

Simulated maps and example TEM cross-sectional images with highlighted crystalline grains are shown in Fig 9. The results from the single scan case are more directly comparable as it is difficult to match the conditions between experiments and simulations for the case of multiple scans. Depending on the parameters of the scans - pulse time, scan rate, pulse frequency - each cell may not have received a pulse for every scan, or in some cases may have received pulses with reduced power if they happened to be away from the laser spot center.

## VI. Conclusion

The modelling approach presented here enables simulations of crystallization of a given GST nanostructure - including the void formation that occurs due to volume reduction in the material - during any annealing conditions or electrical programming. Such simulations can be used to design device structures and operating conditions that minimize void formation. The rate equation approach of solving state variables (crystallinity *CD* and void $\varphi$) allows for material properties to be dynamically updated and applied to areas that are constantly changing shape in the simulation, which can be very difficult in a finite element model with static domains. The model captures the nanoscale phenomena of probabilistic nucleation, growth and void formation, it can be applied on device-level or larger scales and can also be integrated alongside other physics in finite-element tools. The crystallization differences between as-deposited and melt-quenched amorphous material are modeled by a rate equation for the incubation period, with parameters based on experimental results and observations, to capture the effect of remaining nuclei in melt-quenched amorphous material. As further experimental results become available, this model can be validated and built upon for more accurate simulations of phase-change devices. For example, the void formation rate, assumed here to be a constant, is likely a function of temperature, stress and crystallization rates.


[1] S. Raoux *et al.*, "Phase-change random access memory: A scalable technology," *IBM J. Res. Dev.*, vol. 52, no. 4–5, pp. 465–480, 2008.

[2] S. W. Fong, C. M. Neumann, and H. P. Wong, "Phase-Change Memory — Towards a Storage-Class Memory," *IEEE Trans. Electron Devices*, vol. 64, no. 11, pp. 4374–4385, 2017.

[3] G. W. Burr *et al.*, "Recent Progress in Phase-Change Memory Technology," *IEEE J. Emerg. Sel. Top. Circuits Syst.*, vol. 6, no. 2, pp. 146–162, 2016.

[4] P. Ashwin, B. S. V. Patnaik, and C. D. Wright, "Fast simulation of phase-change processes in chalcogenide alloys using a Gillespie-type cellular automata approach," *J. Appl. Phys.*, vol. 104, no. 8, p. 084901, Oct. 2008.

[5] K. B. Blyuss, P. Ashwin, A. P. Bassom, and C. D. Wright, "Master-equation approach to the study of phase-change processes in data storage media," *Phys. Rev. E*, vol. 72, no. 1, p. 011607, Jul. 2005.

[6] G. W. Burr *et al.*, "Observation and modeling of polycrystalline grain formation in Ge2Sb2Te5," *J. Appl. Phys.*, vol. 111, no. 10, pp. 104308–104312, 2012.

[7] W. K. Njoroge, H.-W. Woltgens, and M. Wuttig, "Density changes upon crystallization of Ge2Sb2. 04Te4.74 films," *J. Vac. Sci. Technol.*, vol. 20, pp. 230–233, 2002.

[8] G. C. Sosso, G. Miceli, S. Caravati, F. Giberti, J. Behler, and M. Bernasconi, "Fast crystallization of the

phase change compound GeTe by large-scale molecular dynamics simulations," *J. Phys. Chem. Lett.*, vol. 4, no. 24, pp. 4241–4246, 2013.

[9] J. Akola and R. O. Jones, "Binary alloys of Ge and Te: Order, voids, and the eutectic composition," *Phys. Rev. Lett.*, vol. 100, no. 20, pp. 21–24, 2008.

[10] Z. Woods and A. Gokirmak, "Modeling of Phase-Change Memory: Nucleation, Growth, and Amorphization Dynamics During Set and Reset: Part I--Effective Media Approximation," *IEEE Trans. Electron Devices*, pp. 1–6, 2017.

[11] Z. Woods, J. Scoggin, A. Cywar, L. Adnane, and A. Gokirmak, "Modeling of Phase-Change Memory: Nucleation, Growth, and Amorphization Dynamics During Set and Reset: Part II--Discrete Grains," *IEEE Trans. Electron Devices*, pp. 1–7, 2017.

[12] K. Do, D. Lee, D.-H. Ko, H. Sohn, and M.-H. Cho, "TEM Study on Volume Changes and Void Formation in Ge2Sb2Te5 Films, with Repeated Phase Changes," *Electrochem. Solid-State Lett.*, vol. 13, no. 8, p. H284, Aug. 2010.

[13] I.-M. Park *et al.*, "Thermomechanical properties and mechanical stresses of Ge 2 Sb 2 Te 5 films in phase-change random access memory," *Thin Solid Films*, vol. 517, no. 2, pp. 848–852, 2008.

[14] K. F. Kelton, A. L. Greer, and C. V. Thompson, "Transient nucleation in condensed systems," *J. Chem. Phys.*, vol. 79, no. 12, pp. 6261–6276, Dec. 1983.

[15] J. S. Im and H. A. Atwater, "Ion irradiation enhanced crystal nucleation in amorphous Si thin films," *Appl. Phys. Lett.*, vol. 57, no. 17, pp. 1766–1768, Oct. 1990.

[16] V. Weidenhof, I. Friedrich, S. Ziegler, and M. Wuttig, "Laser induced crystallization of amorphous Ge2Sb2Te5 films," *J. Appl. Phys.*, vol. 89, no. 6, pp. 3168–3176, Mar. 2001.

[17] H.-Y. Cheng, S. Raoux, and Y.-C. Chen, "The impact of film thickness and melt-quenched phase on the phase transition characteristics of Ge2Sb2Te5," *J. Appl. Phys.*, vol. 107, no. 7, p. 074308, Apr. 2010.

[18] B.-S. Lee *et al.*, "Nanoscale nuclei in phase change materials: Origin of different crystallization mechanisms of Ge2Sb2Te5 and AgInSbTe," *J. Appl. Phys.*, vol. 115, no. 6, p. 63506, 2014.

[19] K. Darmawikarta, S. Raoux, P. Tchoulfian, T. Li, J. R. Abelson, and S. G. Bishop, "Evolution of subcritical nuclei in nitrogen-alloyed Ge $_2$ Sb $_2$ Te $_5$," *J. Appl. Phys.*, vol. 112, no. 12, p. 124907, Dec. 2012.

[20] R. M. Shelby and S. Raoux, "Crystallization dynamics of nitrogen-doped Ge2Sb2Te5," *J. Appl. Phys.*, vol. 105, pp. 104902–2849, 2009.

[21] A. Cywar, "Melting and Crystallization of Si and Ge2Sb2Te5 Nanostructures," *Dr. Diss.*, Jan. 2016.

[22] W. Zhang, S. A. Song, H. S. Jeong, J. G. Kim, and Y. J. Kim, "Dislocations in Phase-Change Ge2Sb2Te5 Alloy," *Adv. Mater. Res.*, vol. 26–28, pp. 1097–1100, 2007.

[23] M. H. Jang, K. S. Jeong, S. J. Park, S. J. Park, M.-H. Cho, and J. Y. Song, "Phase-change-induced martensitic deformation and slip system in GeSbTe," *RSC Adv.*, vol. 5, no. 45, pp. 35792–35800, Apr. 2015.

[24] E. Bringa, S. Traiviratana, and M. Meyers, "Void initiation in fcc metals: effect of loading orientation and nanocrystalline effects," *Acta Mater.* , vol. 58, pp. 4458–4477, 2010.

[25] R. E. Rudd, "Void growth in bcc metals simulated with molecular dynamics using the Finnis–Sinclair potential," *Philos. Mag.*, vol. 89, no. 34–36, pp. 3133–3161, Dec. 2009.

[26] R. Fallica *et al.*, "Thermal and Electrical Characterization of Materials for Phase-Change Memory Cells," *J. Chem. Eng. Data*, vol. 54, no. 6, pp. 1698–1701, 2009.

[27] R. Endo *et al.*, "Electric resistivity measurements of Sb2Te3 and Ge2Sb2Te5 melts using four-terminal method," *Jpn. J. Appl. Phys.*, vol. 49, no. 6, p. 5802, 2010.

[28] H. K. Lyeo *et al.*, "Thermal conductivity of phase-change material GeSbTe," *Appl. Phys. Lett.*, vol. 89, p. 151904, 2006.

[29] B.-S. Lee, J. R. Abelson, S. G. Bishop, D.-H. Kang, B. Cheong, and K.-B. Kim, "Investigation of the optical and electronic properties of Ge2Sb2Te5 phase change material in its amorphous, cubic, and hexagonal phases," *J. Appl. Phys.*, vol. 97, no. 9, p. 093509, May 2005.

[30] A. Cywar, J. Li, C. Lam, and H. Silva, "The impact of heater-recess and load matching in phase change memory mushroom cells," *Nanotechnology*, vol. 23, no. 22, p. 225201, 2012.

[31] A. Faraclas, N. Williams, A. Gokirmak, and H. Silva, "Modeling of set and reset operations of phase-change memory cells," *IEEE Electron Device Lett.*, vol. 32, no. 12, pp. 1737–1739, 2011.